Solar Energy Materials & Solar Cells 309 (2027) 114732

Contents lists available at ScienceDirect

Solar Energy Materials and Solar Cells

journal homepage: www.elsevier.com/locate/solmat

Effect of luminescent coupling on current mismatched multijunction photonic power converters

D. Paige Wilson [a,*], Gavin P. Forcade [b], Richard Nacke [c], Jonas Schön [c,d], Carmine Pellegrino [c], Robert F.H. Hunter [a], Oliver Höhn [c,d], Henning Helmers [c], Alexandre W. Walker [b,e], David Lackner [c], Jacob J. Krich [b], Karin Hinzer [a,b]

[a] SUNLAB, Nexus for Quantum Technologies Institute, School of Electrical Engineering and Computer Science, University of Ottawa, Ottawa, ON, K1N 6N5, Canada
[b] Department of Physics, University of Ottawa, Ottawa, ON, K1N 6N5, Canada
[c] Fraunhofer Institute for Solar Energy Systems ISE, Freiburg, 79110, Germany
[d] Department of Sustainable Systems Engineering (INATECH), University of Freiburg, Emmy-Noether-Str.2, Freiburg, 79110, Germany
[e] Quantum Nanotechnologies Research Centre, National Research Council of Canada, Ottawa, ON, K1K 4P7, Canada

ARTICLE INFO

Keywords:
Photonic power converters
Multijunction devices
III-V photovoltaics
InGaAs
Luminescent coupling
Current mismatch

ABSTRACT

We demonstrate the impact of luminescent coupling on the performance of dual-junction InGaAs photonic power converters under current matched and current mismatched conditions through variations in the absorbing layer thicknesses. Comparison between simulation and experimental devices show good agreement when luminescent coupling is included in the model. Its inclusion is necessary to match the experimentally observed increase in spectral responsivity as a function of internal radiative efficiency. We show that on-substrate devices that are bottom limited benefit more from the effects of luminescent coupling than top limited devices. Also, we demonstrate that luminescent coupling provided an additional 16% absolute boost in efficiency for devices where the top subcell absorbed about 100 times more light than the bottom subcell compared to if the effect is excluded from the model. The difference in behaviour between top and bottom limited devices is due to losses through the rear side of the device. Losses can be mitigated by including a planar back reflector, which further improves performance. Increases in efficiency of over 5% absolute are possible for devices designed with a back reflector compared to the same design on-substrate. We show that including a back reflector also improves reabsorption across the device. These efficiency gains indicate that luminescent coupling is a significant process in these devices and its inclusion necessary for accurate device modelling.

1. Introduction

Photonic power converters (PPCs) are photovoltaic devices that convert monochromatic light into electrical power. Photonic power converters share many of the design principles of multi-junction solar cells, but their absorber layers typically consist of a single material. They act as the receiving component in power-by-light systems, which have applications in free-space optical communications and wireless power transmission [1], [2]. Typical use cases require output voltages of up to 5 V. Increased output voltage can be achieved by fabricating multi-junction devices with each subcell of the device connected in series by a tunnel diode. High performing PPCs are current matched, with each subcell absorbing $1/N^{th}$ of the incoming light where N is the number of subcells in the device [2], [3]. They are often fabricated as a vertically segmented stack and current matching is achieved by tailoring the layer thickness of the absorbing material in each subcell [4]. For ternary and quaternary III-V materials both the material composition and the thickness may be tuned to achieve the desired absorption profile while maintaining current matching, a principle similar to what is done for multijunction solar cells [5], [6].

In high-quality III-V materials, radiative recombination is the dominant carrier recombination mechanism. In fact, in the fundamental thermodynamic limit radiative recombination is the only recombination process which is considered [7], [8]. As PPC and multi-junction solar cell performance continues to improve over time and devices tend towards this fundamental limit effects related to radiative events will need to be considered with care [9], [10].

A photon emitted by a radiative process may be reabsorbed

* Corresponding author.
E-mail address: pwilson3@uottawa.ca (D.P. Wilson).

https://doi.org/10.1016/j.solmat.2026.114732
Received 24 June 2026; Received in revised form 27 August 2026; Accepted 23 September 2026
Available online 1 October 2026
0927-0248/© 2026 The Authors. Published by Elsevier B.V. This is an open access article under the CC BY-NC-ND license (http://creativecommons.org/licenses/by-nc-nd/4.0/).

elsewhere in the device. When the photon is reabsorbed within the same subcell, we refer to this process as photon recycling, and when it is reabsorbed in a different subcell, the process is known as luminescent coupling. Both processes can contribute to open circuit voltage enhancement with photon recycling contributing to the largest increase [11]. Luminescent coupling improves current matching between the subcells [12], [13] and reduces wavelength sensitivity [14] by redistributing photocurrent between subcells. Light trapping techniques such as texturing and planar back reflectors have also been employed to improve reabsorption of these radiatively generated photons [15]. These techniques improve optical path length and will also impact where photons are emitted and reabsorbed.

Unlike in multi-junction solar cells, where luminescent coupling can only proceed from absorbers with a larger bandgap energy to a smaller bandgap energy, in PPCs all absorbers have the same bandgap energy so reabsorption can occur between any combination of subcells. These additional pathways increase the importance of photon management throughout the device. For example, light-trapping techniques such as back reflectors and texturing become important elements for redirecting photons towards the top of the PPC [13].

A rigorous treatment of both luminescent coupling and photon recycling in device modelling requires calculating the reabsorption due to radiative recombination at each point across the device self-consistently with the drift-diffusion equations [16], [17]. The added computational complexity of luminescent coupling means that it is often excluded from device modelling or included using simplified models. Partial accounting of the reabsorption of photons produced from radiative recombination events has involved including the effects of photon recycling only [18], effectively increasing the carrier radiative lifetimes, limiting luminescent coupling to adjacent junctions only [14], or by using equivalent diode models [19]. These simplified models can obscure the underlying physics of the effect.

Experimental quantification of luminescent coupling can be challenging as the number of subcells increases. The effects of luminescent coupling scales with irradiance, increasing with the radiative recombination rate. In devices that are current mismatched this process can be observed as an increasing spectral responsivity with irradiance as the total device current is increased due to luminescent coupling [13], [20], [21]. Replication of this rate of change is important when modelling these devices to produce accurate simulations across a wide range of experimental incident powers. The impact of luminescent coupling on the current mismatch can be controlled experimentally by applying an additional bias light to one of the subcells to push the device away from the current matching point. Controlling the mismatch in this way allows coupling effects to be investigated and the technique can be applied to a variety of photovoltaic devices [22], [23], [24]. In PPCs, where each subcell consists of identical absorber material, distinguishing the contributions to each subcell is complex due to multiple possible pathways. These additional pathways make it challenging to isolate the effect of luminescent coupling between any pair of subcells when the total number of subcells is greater than two. In this context, modelling and simulation can be effective tools for understanding the luminescent coupling process and its impact on device performance. It can also aid in differentiating the various physics in experimental devices by turning on and off physical processes in the simulation and comparing the effects.

In this paper we investigate luminescent coupling in vertically stacked InGaAs PPCs designed for wavelengths near 1520 nm. A schematic of the device is shown in Fig. 1. We quantify the impact that internal radiative efficiency (IRE), adjusted through variations in the non-radiative recombination lifetime, can have on device performance and the strength of luminescent coupling effects. We examine these effects under varying degrees of current mismatch with a focus on layer thickness as the key parameter.

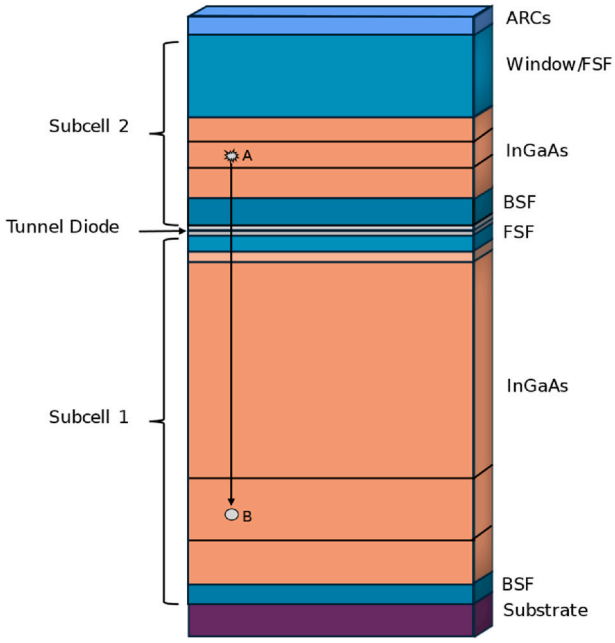

Fig. 1. Schematic of a dual-junction PPC consisting of two subcells. Both subcells consist of InGaAs absorber layers, cladded by higher bandgap front surface field (FSF, highly n-doped) and back surface field (BSF, highly p-doped) layers. The subcells are interconnected in series via a tunnel diode consisting of a p++/n++ junction and cladding layers. A photon emitted from one subcell (A) can be absorbed by the other one (B) as indicated by the arrow. Our model assumes lateral symmetry with variation in element width occurring along the vertical axis (indicated with dotted lines).

2. Methods

2.1. Device modelling with luminescent coupling

Device simulations are performed using a two-dimensional drift-diffusion model in Synopsys Sentaurus TCAD (version S-2021.06, Mountain View, CA, USA). The spectrally integrated radiative recombination rate R_A in a small element A of the device is related to the generation rate G_B in another element B of the device by a coupling coefficient:

$$C_{AB} = \frac{G_B V_B}{R_A V_A} \tag{1}$$

where V_A and V_B are the volumes of elements A and B, respectively.

The coupling coefficient, C_{AB}, between each element in the device depends only on the optical properties of the layer stack. Once this quantity is known for every combination of elements in the device, it can be used in the drift-diffusion simulation to self-consistently calculate the radiative recombination and total generation rates throughout the device. The coupling coefficient is calculated using the transfer matrix method (TMM) with an internal electric field source as described in Ref. [17]. While the calculation of luminescent coupling used in this work follows the same logical structure as that in Ref. [17] several improvements have been made to stability which improve performance and prevent overestimating the contribution of luminescent coupling. In particular, suppression of large values as the angle of emission approaches $\pi/2$ led to improved agreement with photon recycling models and suppressing undefined quantities, a common issue in angle dependent calculations as has been noted elsewhere [25]. A discussion of our method is given in the Supplementary Information and the code has been made available in an open-source repository [26]. This calculation assumes a laterally uniform device with planar layers stacked along the z direction. Since all points in the device are considered, both luminescent

coupling (coupling to other subcells) and photon recycling (inside one subcell) are represented. Considering all internal emission angles and a range of emission energies the expression for the coupling coefficient is:

$$\frac{C_{AB}}{V_B} = \frac{1}{4W}\frac{1}{L_B}\int_0^{L_B}\int_0^{\infty}\int_0^{\pi}[a_{TE}(\theta,E,z)+a_{TM}(\theta,E,z)]sin\,\theta\widehat{S}(E)d\theta dEdz \quad (2)$$

where W is the width or area of the device (for 2D or 3D simulations respectively), L_B is the length of element B, E is the emission photon energy, and θ is the angle of emission. The quantities a_{TE} and a_{TM} are the absorption densities associated with element B for the transverse electric (TE) and transverse magnetic (TM) polarizations respectively and are calculated from the TMM electric field solutions. They are absorption events per unit distance, emission angle, and emission energy and have dimensions of 1/length/angle/energy. The $sin\,\theta$ normalizes the expression over angle, and $\widehat{S}(E)$:

$$\widehat{S}(E) = \frac{\alpha(E)n_r^2(E)E^2\exp\left(-\frac{E}{kT}\right)}{\int_0^{\infty}\alpha(E)n_r^2(E)E^2\exp\left(-\frac{E}{kT}\right)dE} \quad (3)$$

is the normalized van Roosbroek-Shockley expression for the spectral distribution of radiative recombination. $\widehat{S}(E)$ gives the distribution of the emitted photons with respect to their energy [17], [18], [27], [28], [29]. Here α is the absorption coefficient of the emitting material, n_r is the complex refractive index of the emitting material, T is the temperature, and k is the Boltzmann constant. We assume no absorption below the band-edge. Similar assumptions have been made in Refs. [16], [17] and [25].

2.2. Device model

A drift-diffusion calculation is performed within Synopsys Sentaurus TCAD. The absorption of the incident laser light throughout the layer stack is calculated with S^4 which uses rigorous coupled wave analysis (RCWA) [30]. The refractive index of the InGaAs absorber layers was extracted experimentally from ellipsometry measurements using single junction isotypes of the InGaAs material. The absorption coefficients were obtained from external quantum efficiency and reflectance measurements [31].

The radiative recombination rate is described by $R_{rad} = B_{rad}\left(np - n_{i,eff}^2\right)$ with the radiative recombination coefficient, B_{rad}, calculated from Refs. [18], [28]:

$$B_{rad} = \frac{8\pi q}{3hc^2n_i^2}\int_0^{\infty}\frac{\alpha(E)n_r^2(E)\,E^2}{\exp\left(\frac{E}{kT}\right)-1}dE \quad (4)$$

which is the integral of the van Roosbroek-Shockley equation divided by n_i^2, where q is the electric charge, h is Plank's constant, and c is the speed of light in vacuum. This expression results in a value of 2×10^{-10} cm^3/s for the p-type InGaAs absorber region which is within the same order of magnitude reported elsewhere [32], [33]. Where the photon-recycling only model is employed, B_{rad} is reduced by an additional photon recycling factor in each layer as described in Ref. [18]. Where the luminescent coupling model is used to calculate contributions from self-absorption throughout the entire device, B_{rad} is not directly altered.

The Shockley-Read-Hall (SRH) carrier lifetimes in the absorber layers use the built-in Scharfetter model in Sentaurus which adjusts the carrier lifetimes based on the doping in each region of the device according to:

$$\tau_{n,p} = \frac{\tau_{max,np}}{1+\left(\frac{N_{A0}+N_{D0}}{N_{ref}}\right)^{\gamma}} \quad (5)$$

where N_{A0} and N_{D0} are the acceptor and donor concentrations in p- and n-type materials respectively [31]. The reference concentration, N_{ref}, is set as 1×10^{16} cm^{-3} and γ is set to 1.5 for both carrier types. The lifetimes in the low concentration limit for each carrier type, $\tau_{max,np}$, are adjusted independently to determine the impact on device performance as a function of material quality as discussed in Section 3.1.

Additional physics that are considered in the model include Auger recombination, thermionic emission at heterojunctions, and charge carrier tunneling at the tunnel diodes. More details on the model physics can be found in Ref. [31].

2.3. Experimental details

Dual-junction InGaAs based PPCs, lattice matched to an InP substrate, were grown by metal-organic vapour phase epitaxy using an Aixtron G4 2800TM reactor. Each subcell's InGaAs absorber layers, with thicknesses of 1 μm and 2 μm in the top and bottom subcells respectively, are cladded by highly doped front and back surface field layers, which are transparent to 1520 nm light. The two subcells are connected via a tunnel diode. Standard metal contacts are deposited on front and rear side. An anti-reflection coating is deposited on the front surface and is designed for wavelengths near 1520 nm. Individual devices are separated via chemical wet-etching. The mesa area is about 2.2 mm × 2.9 mm, with a total chip area of 6.4 mm^2 (nominal designated area without busbars 5.4 mm^2).

Devices are measured using a 4-point probe setup on a temperature-controlled stage held at 25 °C. The device is illuminated using a Dilas high-power fiber-coupled laser temperature-tuned to 1520 nm. The light emitted from the fiber is collimated and then focused to a spot size just narrower than the dimensions of the device to avoid spillage losses but not so small as to create unwanted conduction losses and localized heating effects [34]. The power of the incident laser P_{in} is measured using a thermopile and calibrated by comparing the responsivity of single junction isotype devices. The power is adjusted by changing the drive current of the laser. Further adjustments can be made by inserting neutral density (ND) filters into the path of the beam. These filters are absorptive, and we observe heating effects that allow increasing amounts of light to transmit through the filter over the course of the few seconds required for the thermopile to stabilize. To correct for these effects, we apply experimentally determined correction factors to the filter power equal to 0.988 for our ND1 filter and 0.985 for our ND2 filter to maintain continuity with the results when no filters are present.

3. Results and discussion

3.1. Effect of material quality in the presence of luminescent coupling

Luminescent coupling is expected to play a strong role in the performance of devices which are current mismatched. In these cases, redistribution of photons between subcells aids in bringing the devices closer to current matched conditions. We perform J-V measurements on a PPC designed to be current mismatched with the bottom layer limiting the current. For a single pass, the thicknesses of the top and bottom subcells result in 56% of the incoming light at 1520 nm being absorbed in the top subcell and 36% being absorbed in the bottom subcell with the difference being transmitted based on Beer-Lambert absorption. Note that despite current mismatch, at short circuit the J-V curves do not show any sign of subcell breakdown. Thus, we extract the responsivity of the device at short circuit as a function of the incident irradiance: $SR = J_{sc}/P_{in}$. This value is an important indicator of the strength of luminescent coupling within a device under normal operating conditions. Fig. 2 shows the experimentally measured responsivity of the current mismatched PPC. We observe a nonlinear change in the responsivity with respect to the incident irradiance. The decrease in responsivity at the highest irradiances is attributed to sample heating.

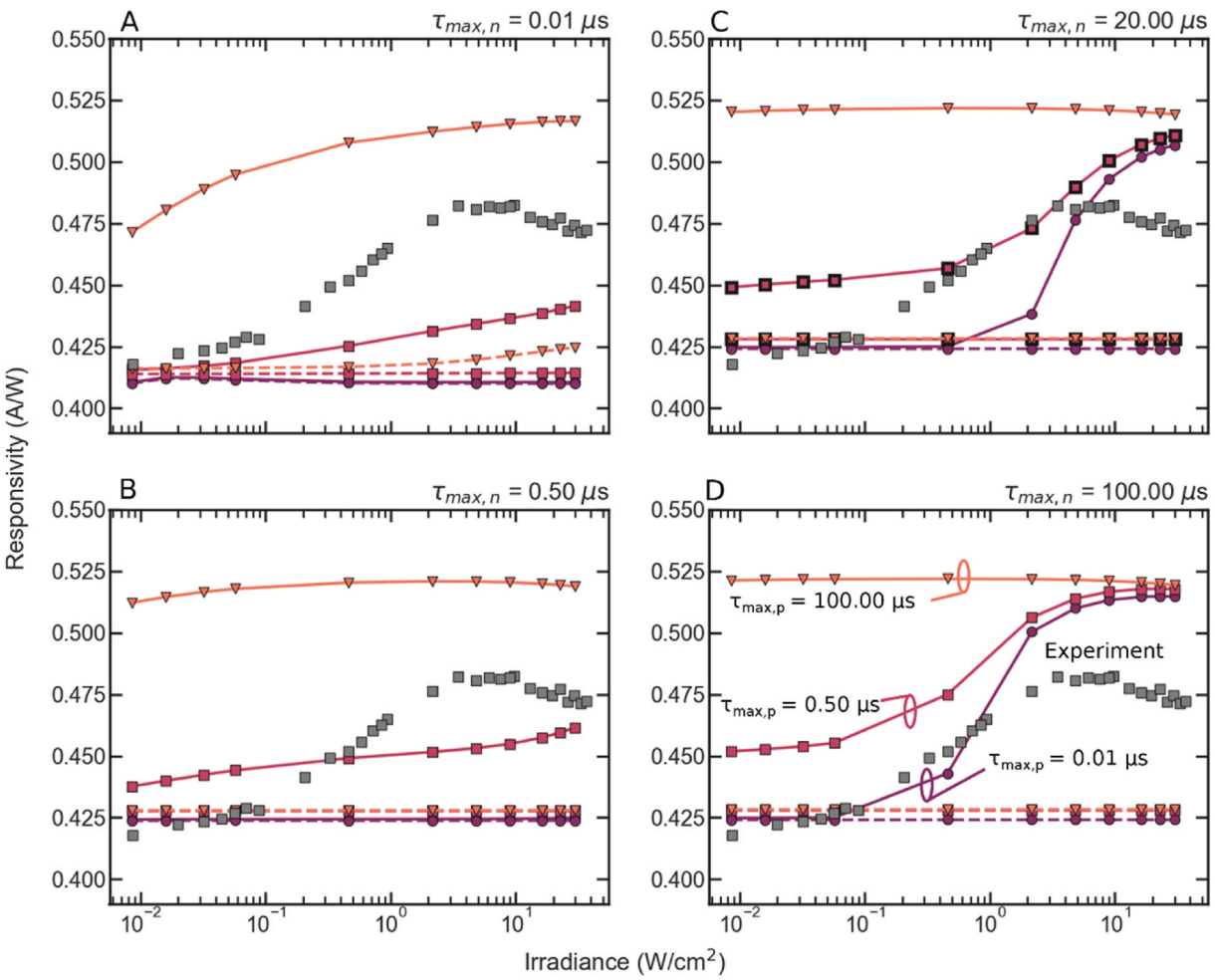

Fig. 2. Modeled responsivity of a bottom limiting dual-junction PPC at 1520 nm as a function of incident irradiance (colored symbols.) The responsivity of an experimental device (C5195-X29Y8) of the same nominal thickness as simulated is shown for comparison (gray squares.) Different colors and markers represent different hole lifetimes $\tau_{max,p}$, and the four subplots vary in their electron lifetimes $\tau_{max,n}$. In each plot, two models are compared: one which includes the effects of luminescent coupling between layers (solid lines) and one which only considers photon recycling within a single layer (dashed lines). The bolded square markers in the top right plot indicate values used for the remainder of this paper.

Note that with increasing temperature the bandgap energy of the absorbers is reduced and thus the top subcell absorptivity increases. This increase in J_{sc} due to decreased bandgap energy with temperature is not expected to be strong enough to yield the rate of responsivity increase observed in Fig. 2. The impact of sample heating could be reduced by performing the voltage sweeps with a rapid scan rate (on the order of ms or smaller) or by using a pulsed voltage scan. In each case the laser exposure and measurement should be synced to minimize the time the sample spends under direct illumination.

While the nonlinear responsivity with respect to incident irradiance can be attributed in part to luminescent coupling, we find that the rate of change observed experimentally cannot be explained by this effect alone. To better reproduce the experimental behaviour in our model we adjust the internal radiative efficiency, defined as the fraction of recombination events that are radiative throughout the entire device:

$$IRE = \frac{\int R_{rad} dz}{\int \left(R_{Rad} + R_{Aug} + R_{SRH}\right) dz} \tag{6}$$

where R_{Rad}, R_{Aug}, and R_{SRH} are the rates of radiative, Auger, and Shockley-Read-Hall recombination respectively. The IRE is adjusted by changing the SRH lifetimes within the absorber layers according to Eq. (5) by adjusting $\tau_{max,np}$ for both carrier types. Fig. 2 shows the impact that changing the SRH lifetime has on the responsivity of a dual-junction InGaAs PPC under 1520 nm incident irradiance when full luminescent coupling effects (solid lines) or only photon recycling effects (dashed lines) are included in the simulation.

We observe two bounding limits to the responsivity of the device. For a given pair of SRH lifetimes the photon recycling only model provides lower responsivity than the luminescent coupling model due to the advantageous redistribution of current when luminescent coupling is included in the model for current-mismatched devices. For both models, short SRH lifetimes increase the responsivity with respect to irradiance up to a maximum value (for example, see panel A of Fig. 2). For longer SRH lifetimes i.e. higher radiative efficiency, the responsivity increases to its maximum value at a lower irradiance. These trends are present for both models but are accentuated when luminescent coupling is included in the model. For the longest lifetimes considered here the photon recycling only model gives a constant responsivity regardless of irradiance (panel D). When luminescent coupling is included, the lower boundary is given by the photon recycling model's upper bound. The significance of this is that luminescent coupling between different subcells of a device will increase or provide no change to the short circuit current of the device but will not decrease the short circuit current, compared to if the coupling effect is not considered.

The luminescent coupling model also shows a much greater dependence of the responsivity on the irradiance, which is reflected in the experiment. For short lifetimes, IRE is small so there is little luminescent

coupling, which is demonstrated by the two models converging onto the lower valued photon recycling curves. For long lifetimes, the responsivity approaches its upper limit at all considered irradiances (panels C and D for $\tau_{max,p} = 100\ \mu s$) appearing almost constant over the irradiance values considered in Fig. 2 and corresponding to an IRE approaching 1. For intermediate lifetimes there is a transition between the lower and upper responsivity bounds as the irradiance is increased (panels C and D for $\tau_{max,p} = 0.5\ \mu s$.) Shorter lifetimes require higher irradiances to increase the responsivity (for panels C and D and $\tau_{max,p} = 0.01\ \mu s$).

Irradiance-dependent responsivity occurs in our modeling due to the injection dependence of the recombination rates within the device. Experimentally, this dependence is attributed to increasing IRE as trap states saturate with increased carrier injection [28], which are accounted for in our modelling through the standard expression for SRH recombination and assuming deep-level trap states at mid-gap. Under high-injection conditions, electron and hole populations become equal, independent of doping levels, and the SRH lifetime becomes the sum of the majority and minority carriers rather than being limited by the minority carrier lifetime [28], [35] and these populations dominate over the trap-state concentration. In the same limit, the radiative recombination rate is proportional to n^2 while the SRH rate is proportional to n [31] so, IRE increases with irradiance and the responsivity approaches an upper bound as IRE approaches 1.

Fig. 3 further demonstrates the relationship between responsivity and IRE. To facilitate a more complete understanding of the results of Fig. 2, the responsivity is plotted against the IRE with the change in irradiance becoming rolled into this value. In this figure the direct relationship between the responsivity and the internal radiative efficiency is apparent as the different curves collapse onto each other, and the deviations owing to different lifetimes and irradiance conditions can be described by a single dependent variable, the internal radiative efficiency. These plots support our understanding of the plateaus and slopes for the luminescent coupling model results in Fig. 2. For short SRH lifetime and/or low irradiance the IRE is low and recombination is dominated by SRH recombination which prevents photon recycling and luminescent coupling and thus the responsivity remains constant. Increasing IRE allows radiative recombination to dominate over SRH. In such cases luminescent coupling produces a change in the responsivity of the device as it reduces the current mismatch. As IRE approaches its upper limit of 1, the effects of luminescent coupling saturate, with no further improvements to current mismatch, resulting in the second region of constant responsivity observed in Fig. 2 in the high irradiance and/or long SRH lifetime limits. For modelling with only photon recycling the responsivity remains constant regardless of the IRE and strength of the radiative recombination since photon exchange between subcells has been neglected and thus total device current is unchanged. From these plots it is also apparent that matching the non-constant experimental responsivity of the devices requires that both luminescent coupling and IRE be accounted for since the photon recycling model does not show a strong rate of change as the IRE is altered. In addition, for the same irradiance values, the model which includes luminescent coupling shows increased IRE for the same levels of irradiance when compared to the photon recycling only model, as indicated by the shifting of the luminescent coupling curves to the right side of the plot.

For the remainder of our modelling, we select 20 μs and 0.5 μs for $\tau_{max,n}$ and $\tau_{max,p}$ respectively. While these values do not agree precisely with the experimental data they produce a change of slope that is similar to that present in the experimental data even if differences persist at the low irradiance values. We deem the slope change at the mid-irradiances to be of greater interest to this study, rather than the upper and lower extremes. A more precise fit to the experimental data could be obtained by performing a best fit optimization which is beyond the scope of the present study. The responsivity associated with these values are indicated by the bolded square markers in panel C of Fig. 2 and in Fig. 3. The SRH lifetimes resulting from these maximum-lifetime parameters in accordance with Eq. (5) and the doping are shown in Supplementary Fig. S1. Plots comparing the *J-V* curves of the simulations using the SRH dependent lifetimes with experimental data for the bottom limiting device are shown in Fig. 4. There is good agreement between the experiment and simulated device that includes luminescent coupling up until the highest irradiances, where heating effects limit the experimental device performance. The device simulated with only photon recycling effects produces lower currents than shown in the experiment due to the lower overall responsivity and its constant nature with respect

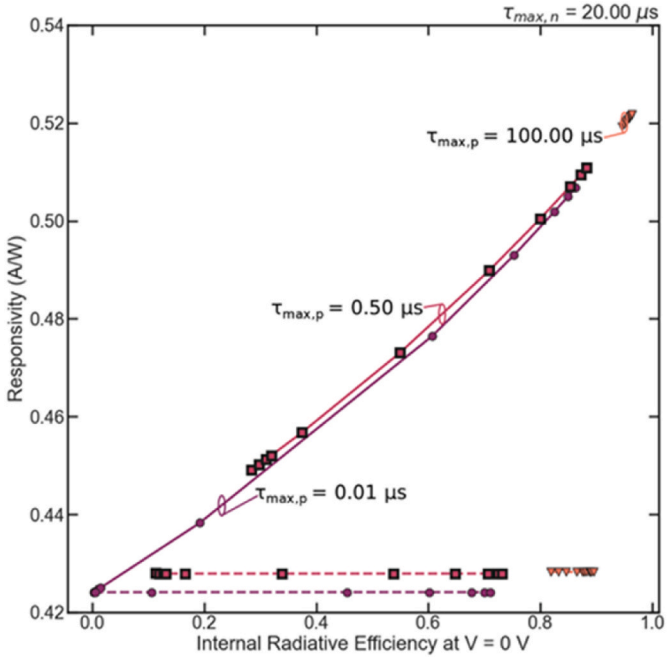

Fig. 3. Responsivity of a bottom limiting dual-junction PPC at 1520 nm as a function of the internal radiative efficiency under short-circuit conditions. The responsivity at 1520 nm is shown for various effective Shockley-Read-Hall lifetimes as governed by Eq. (5) and produced by varying the values of $\tau_{max,np}$ in different combinations. In each plot, two models are compared: one which includes the effects of luminescent coupling between layers (solid lines) and one which only considers photon recycling within a single layer (dashed lines).

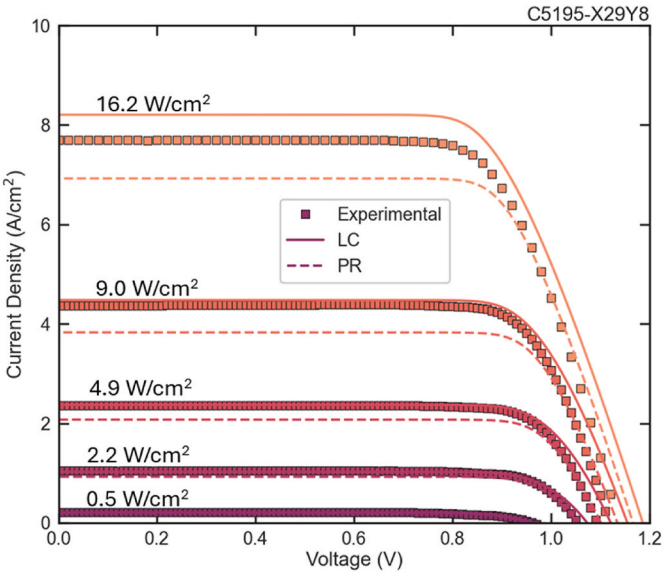

Fig. 4. Current density vs. voltage curves for a simulated dual-junction device (solid and dashed lines) and experimental measurements (square symbols).

to irradiance for the lifetime values selected.

In addition to the effects discussed in this work, other irradiance dependent behaviour has been observed in multijunction devices with the cause being attributed to different sources. For example, measurements and modelling of multijunction photovoltaic devices have demonstrated this behaviour owing to low shunt resistance and/or low reverse breakdown voltages of one or more subcells [19], [23], [36]. Another possible source could be unexpected deviations in nominal thickness during growth of the device. These deviations, while small, could become more apparent as the number of junctions increases. Contributions from multiple effects could contribute to a rise in the responsivity of the device that are difficult to distinguish from one another, which underscores the importance of properly modelling important effects such as luminescent coupling to understand device performance.

In Fig. 2 we observe a slight decrease in responsivity at the highest irradiances even when the lifetimes of both carriers are long. This decrease is attributed to the increased prevalence of Auger recombination as high injection conditions are approached. The impact of each type of recombination mechanism on the short circuit current density in the top and bottom subcells is shown in Fig. 5 for both photon recycling and luminescent coupling models. These contributions to the total current are calculated as the integral of each recombination rate over the specified subcell absorber region and multiplied by the electric charge. All quantities in Fig. 5 are plotted as positive values but, to clarify, the luminescent coupling current will add to the current of a subcell while the radiative, Auger, and SRH currents will subtract from it. These quantities are in addition to the photocurrent generated in each subcell due to the incident irradiance which is the largest contribution to the current at short-circuit and is not plotted here for clarity. As the irradiance increases the following can be observed in the behaviour of the top subcell (SC2) for both the luminescent coupling and photon recycling models: 1) the SRH recombination current begins to increase more slowly as IRE increases due to increased injection, 2) the radiative recombination current begins to increase at a faster rate and surpasses the SRH recombination current to become the dominant source of recombination, and 3) Auger recombination becomes more significant and becomes comparable to the SRH recombination at the highest irradiance levels. The transition between non-radiative SRH-dominated recombination and radiative-dominated recombination as the irradiance is increased is significant since it allows a greater number of photons to be emitted, reabsorbed, and collected within the device.

In addition to these general observations, we also compare the photon recycling model and luminescent coupling models directly. When luminescent coupling is included in the model the radiative recombination current in the bottom subcell, which is the largest loss current for the photon recycling model, decreases by orders of magnitude. This lower value better reflects the real-life operating conditions of the individual subcells. Since the total device operates at 0 V, the limiting bottom subcell must be reverse biased while the overproducing top subcell operates in forward bias. Under these conditions the bottom subcell is expected to produce little radiative recombination [37], [38]. We also note that the SRH recombination in the bottom subcell experiences an increase when luminescent coupling is included compared with only photon recycling. This and other minor changes in the recombination currents are due to the different subcell operating conditions and excess current densities that occur between the two models.

3.2. Luminescent coupling in the limit of ultra-thin and ultra-thick absorber layers

The results in section 3.1 indicate improvements to the responsivity of a bottom limiting InGaAs PPC due to current redistribution through luminescent coupling. In the case already explored, the current mismatch between the subcells was due to the top subcell being too thick relative to the bottom subcell resulting in more photons being absorbed in the top subcell than the bottom subcell. In this section we explore the impact of current mismatch in device performance due to relative changes in the thickness of the absorbing layers. We define the absorption ratio as the amount of light absorbed in the top subcell over the amount of light absorbed in the bottom subcell, $a_{ratio} = a_{top}/a_{bot}$, for a given wavelength. By this definition an $a_{ratio} > 1$ corresponds to a device which is bottom limited and an $a_{ratio} < 1$ corresponds to a device which is limited by the top subcell. The absorption ratio is calculated based on the single-pass Beer-Lambert absorption in each subcell and neglects multiple reflections and luminescent coupling.

Fig. 6 shows the short-circuit current, open-circuit voltage, fill factor, and efficiency for dual-junction PPCs at three incident irradiances. The absorption ratios were obtained by holding the sum of the two absorber thicknesses constant at 4.83 μm, which results in 98% of the incident 1520 nm light being absorbed within the device, while altering the thicknesses of the individual absorber layers. The difference in magnitude between the two models on the left- and right-hand sides of $a_{top}/a_{bot} = 1$ indicate that luminescent coupling has a lower impact on devices which are limited by the top subcell. The effect has a much stronger impact on the device performance when the bottom subcell limits. In this case, luminescent coupling provides a significant improvement to both the short circuit current and the open circuit

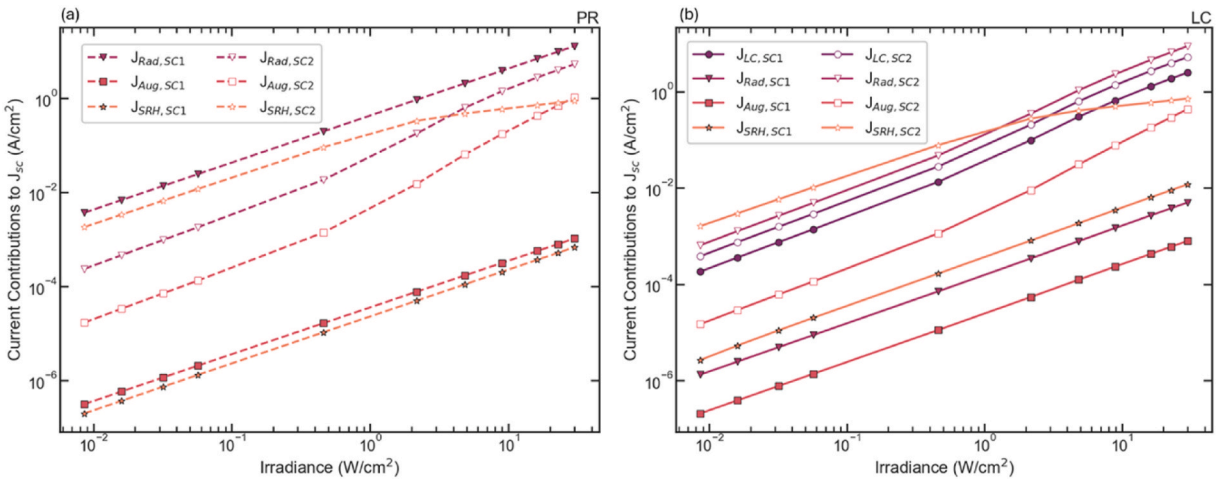

Fig. 5. The currents in the bottom subcell (SC1, closed markers) and top subcell (SC2, open markers) owing to radiative recombination, J_{rad}, Auger recombination, J_{Aug}, and Shockley-Read-Hall recombination, J_{SRH} when (a) only photon recycling effects are included in the model and when (b) full luminescent coupling is considered. When luminescent coupling is included in the modelling there is additional contribution to the current in each subcell, J_{LC}, indicated in (b).

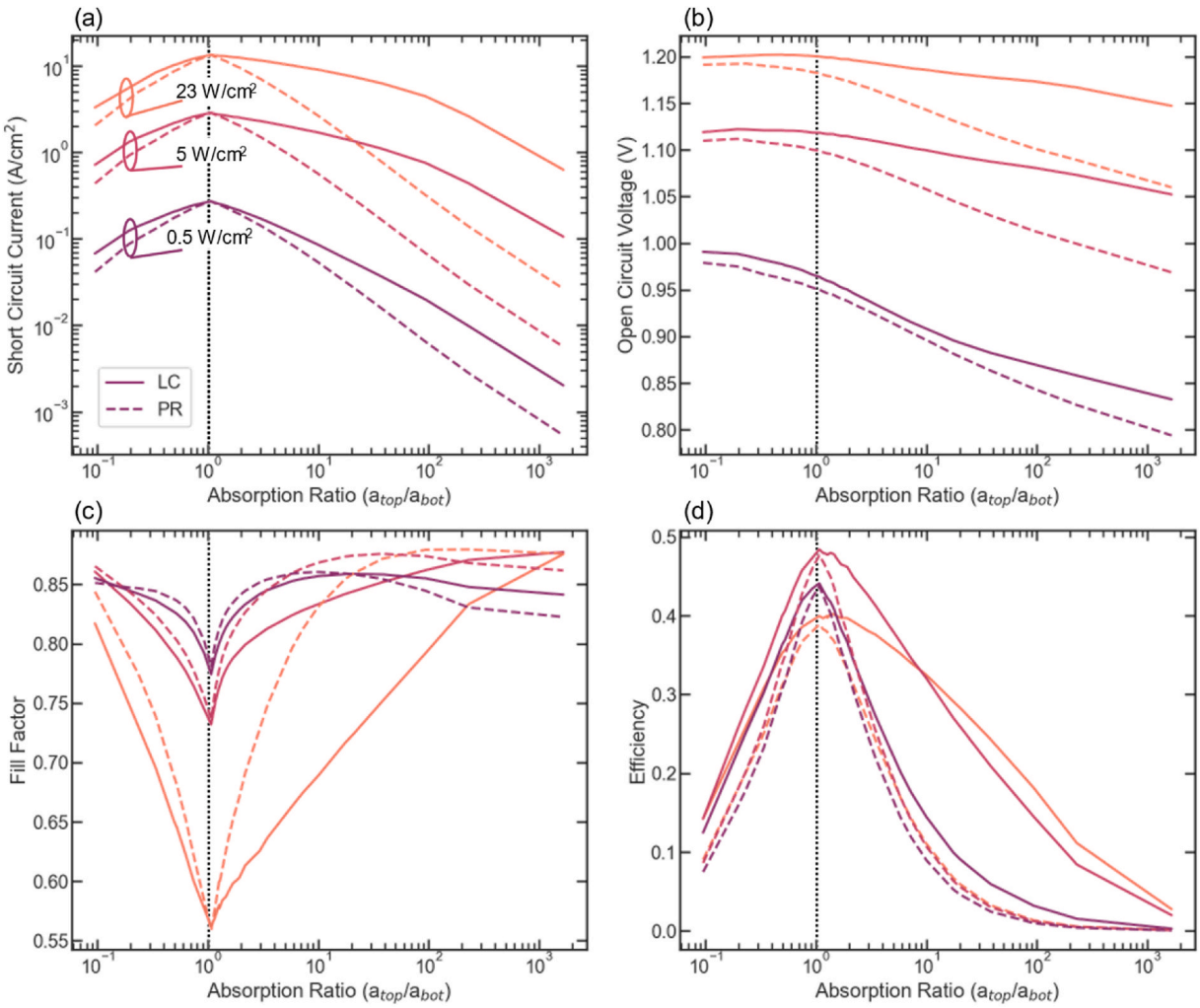

Fig. 6. The (a) short circuit current density (J_{sc}), (b) efficiency, (c) fill factor (*FF*), and (d) open circuit voltage (V_{oc}) of dual-junction photonic power converters with luminescent coupling included in the model (solid lines) and with luminescent coupling excluded from the model (dotted lines) as a function of the absorption ratio due to changes in relative thickness of the top and bottom subcells. Line colour indicates three different incident irradiances at 1520 nm laser light: 0.5 W/cm^2, 5 W/cm^2, and 23 W/cm^2.

voltage allowing the rate of decay of efficiency with increasing absorption ratio to slow. Even in the extreme limit, for an absorption ratio of 100, the efficiency of the device still shows close to 18% efficiency for the highest irradiance considered when luminescent coupling is present in the model, which is an improvement of about 16% absolute efficiency compared to modelling when it is excluded. This is in line with experimental observations in Ref. [16]. For the total absorber thickness of 4.83 μm considered here, an absorption ratio of 100 would result from a 4.33 μm thick top subcell and a 0.5 μm thick bottom subcell. There is diminishing return on this figure as the ratio between the subcell thicknesses is increased further.

The reason for the significant difference in luminescent coupling contribution in the bottom-limiting vs. top-limiting cases is due to rear-side transmission losses into the substrate. Without a back reflector present, photons emitted in the bottom subcell towards the rear side of the device are lost to transmission into the substrate. This loss peaks at 50% of radiative events when the radiative recombination emission location is at the interface between the last layer and the substrate. The transmission losses for radiated photons originating in the top or bottom subcell of the device are shown in Fig. 7 (a) and (b) respectively. In these plots the total thickness of the absorber regions is not fixed and both the bottom and top subcells are allowed to vary. The thickness of the bottom subcell is indicated in the legend and the thickness of the top subcell can be inferred from the absorption ratio, with thinner top subcells tending to the left-hand side of the plot and thicker top subcells tending to the right.

Fig. 7 (a) shows that less than 10% of all radiatively generated photons originating in the top subcell are lost due to transmission into the substrate, indicating that the majority are reabsorbed within the device. More photons are lost to transmission overall as the bottom subcell is thinned and fewer photons are lost if the bottom subcell's thickness is held constant and the top subcell is made thicker. These trends owe to the simple fact that photons are more likely to be reabsorbed within the device as the total path length between their emission point and the rear interface is lengthened.

Fig. 7 (b) shows similar trends for photons originating in the bottom subcell of the device although the overall percentage of losses is in general higher, approaching 15% for the absorption ratios considered here. Again, there is an increase in the percentage of photons transmitted overall as the bottom subcell is thinned. There is little influence on bottom subcell losses as the thickness of the top subcell is changed. This trend is due to upward travelling photons reflecting off the top surface, increasing the overall path length and thereby increasing the likelihood of reabsorption.

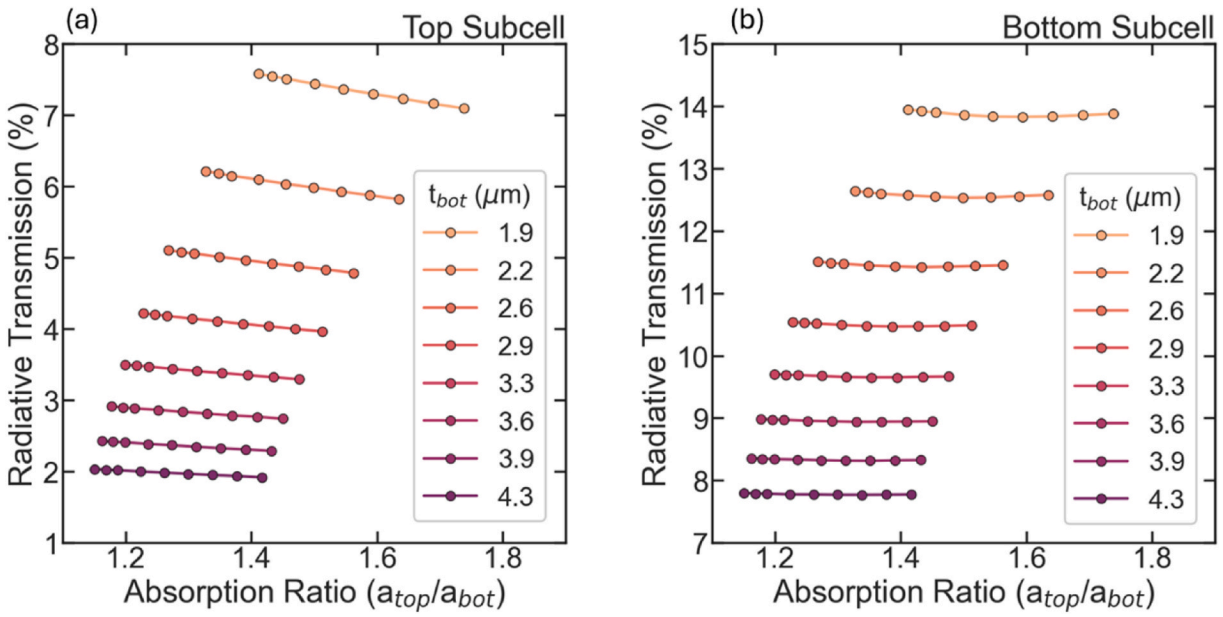

Fig. 7. The percentage of radiative events transmitted through the rear side of the device that originate in (a) the top subcell of the PPC and (b) the bottom subcell of the PPC.

3.3. *Luminescent coupling in the presence of a planar back reflector*

While on-substrate designs are advantageous for their simpler fabrication process, novel and improved techniques are making planar back reflectors and textured rear surfaces more efficient and accessible. In this last analysis, we include a planar, gold back reflector at the rear boundary of the simulated dual-junction PPC. Fig. 8 (a) shows a comparison between the JV curves at different irradiance levels when a back

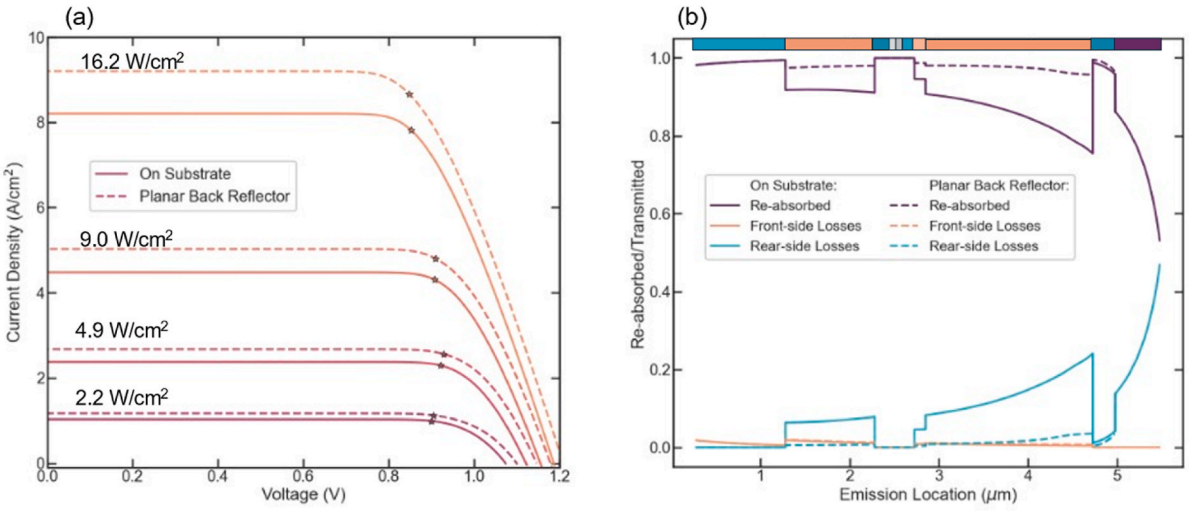

Input Power Density (W/cm²)	On Substrate				Planar Back Reflector			
	J_{sc} (A/cm²)	V_{oc} (V)	FF	Efficiency (%)	J_{sc} (A/cm²)	V_{oc} (V)	FF	Efficiency (%)
2.2	1.03	1.07	0.81	41.10	1.17	1.10	0.79	46.76
4.9	2.38	1.12	0.79	43.54	2.67	1.15	0.78	49.05
9.0	4.48	1.15	0.76	43.65	5.03	1.18	0.74	48.80
16.2	8.20	1.19	0.68	41.17	9.20	1.21	0.66	45.41

Fig. 8. (a) The simulated J-V curves for a dual-junction PPC with and without a planar back reflector present under different incident irradiances. The markers indicate where the maximum power point occurs. (b) The fraction of radiative recombination events which are reabsorbed or transmitted through the front- and read-sides of the device as a function of the emission location of the radiative event. The colored bars at the top of the plot correspond to the different layers as indicated in Fig. 1. The table shows modeled parameters: the short-circuit current density Jsc, open-circuit voltage Voc, fill factor FF, and efficiency for different irradiances.

reflector is and is not present. Fig. 8 (b) shows a comparison of the fraction of radiatively emitted photons that are either reabsorbed, transmitted through the front surface, or transmitted through the rear surface of the active device as a function of their emission location with and without a back reflector incorporated into the design. Fig. 8 utilizes the same representative PPC design shown from Fig. 4.

The inclusion of a planar back reflector increases the fraction of radiatively emitted photons that are reabsorbed within the device. The percentage of photons reabsorbed by the device exceeds 95% in both the bottom and the top subcell absorber regions. This improvement in the number of photons being reabsorbed in the device will strengthen the impact of luminescent coupling within the device allowing for thinner absorbing layers.

4. Conclusions

We demonstrate that luminescent coupling plays an important role in dual-junction PPCs when current mismatch between the subcells is present due to variations in the thicknesses of the absorbing regions of the device. The strength of the luminescent coupling effect is directly related to the IRE of the device, increasing as the IRE increases, an effect which is not observed when only photon recycling effects are included in the model. Experimental results come into good agreement with numerical modelling when luminescent coupling is included underscoring the importance of including the effect in the model since photon recycling alone cannot reproduce these trends.

We show that the positive impact of luminescent coupling within the device is strongest for on-substrate, bottom limiting designs. The mitigation of current mismatch is lower in the top limiting designs considered in this work but still present. The difference in behaviour between bottom and top limiting devices is due to transmission losses into the substrate. This effect can be reduced by including a back reflector in the device design. Inclusion of a back reflector increased the percentage of radiatively emitted photons that are reabsorbed to over 95% in both absorber regions.

From a modelling perspective we suggest that luminescent coupling be included in on-substrate InGaAs PPC models, in particular when the device being simulated is bottom limiting as the effect is significant in this case. Inclusion of the effect avoids underestimating device performance. In top limiting designs, the effect may be excluded at the designer's discretion to save on computational expense.

As a final point, while luminescent coupling is necessary to explain device performance its effect should be considered in the context of other physical effects which impact device behaviour. Additional effects such as injection dependent lifetimes, variations in experimental device thicknesses, and beam non-uniformity will also effect performance, and their relationship to luminescent coupling should be investigated in future work.

CRediT authorship contribution statement

D. Paige Wilson: Writing – review & editing, Writing – original draft, Visualization, Validation, Methodology, Investigation, Formal analysis, Data curation, Conceptualization. **Gavin P. Forcade:** Writing – review & editing, Validation, Methodology. **Richard Nacke:** Writing – review & editing, Validation, Data curation. **Jonas Schön:** Writing – review & editing, Methodology. **Carmine Pellegrino:** Writing – review & editing, Data curation. **Robert F.H. Hunter:** Writing – review & editing, Methodology. **Oliver Höhn:** Writing – review & editing, Project administration, Funding acquisition. **Henning Helmers:** Writing – review & editing, Resources, Project administration, Funding acquisition. **Alexandre W. Walker:** Writing – review & editing, Project administration, Funding acquisition, Conceptualization. **David Lackner:** Writing – review & editing, Resources, Funding acquisition, Data curation, Conceptualization. **Jacob J. Krich:** Writing – review & editing, Funding acquisition, Conceptualization. **Karin Hinzer:** Writing – review & editing, Supervision, Resources, Project administration, Funding acquisition, Conceptualization.

Declaration of competing interest

The authors declare that they have no known competing financial interests or personal relationships that could have appeared to influence the work reported in this paper.

Acknowledgements

This work was supported by the Government of Canada under the High Throughput Secure Network Challenge Program HTSN-645, the Natural Sciences and Engineering Research Council of Canada under grant 497981, CMC Microsystems, the Canadian Foundation for Innovation, a Fraunhofer ICON grant through the project GreenCom, and the German Federal Ministry of Education and Research under grant 01DM21006A.

Appendix A. Supplementary data

Supplementary data to this article can be found online at https://doi.org/10.1016/j.solmat.2026.114732.

Data availability

Data will be made available on request.

References

[1] K. Worms, et al., Reliable and lightning-safe monitoring of wind turbine rotor blades using optically powered sensors, Wind Energy 20 (2) (Feb. 2017) 345–360, https://doi.org/10.1002/we.2009.
[2] H. Helmers, et al., Photovoltaic cells with increased voltage output for optical power supply of sensor electronics, in: AMA Conferences 2015, AMA Service GmbH, Dec. 2015, pp. 519–524, https://doi.org/10.5162/sensor2015/d1.4.
[3] J. Schubert, E. Oliva, F. Dimroth, W. Guter, R. Loeckenhoff, A.W. Bett, High-voltage GaAs photovoltaic laser power converters, IEEE Trans. Electron. Dev. 56 (2) (2009) 170–175, https://doi.org/10.1109/TED.2008.2010603.
[4] C.E. Valdivia, et al., Five-volt vertically-stacked, single-cell GaAs photonic power converter, in: Physics, Simulation, and Photonic Engineering of Photovoltaic Devices IV, SPIE, Mar. 2015, p. 93580E, https://doi.org/10.1117/12.2079824.
[5] R.M. France, et al., Design flexibility of ultrahigh efficiency four-junction inverted metamorphic solar cells, IEEE J. Photovoltaics 6 (2) (Mar. 2016) 578–583, https://doi.org/10.1109/JPHOTOV.2015.2505182.
[6] S.R. Kurtz, P. Faine, J.M. Olson, Modeling of two-junction, series-connected tandem solar cells using top-cell thickness as an adjustable parameter, J. Appl. Phys. 68 (4) (1990) 1890–1895, https://doi.org/10.1063/1.347177.
[7] A. Martí, G.L. Araújo, Limiting efficiencies for photovoltaic energy conversion in multigap systems, Sol. Energy Mater. Sol. Cell. 43 (2) (1996) 203–222.
[8] W. Shockley, H.J. Queisser, Detailed balance limit of efficiency of p-n junction solar cells, J. Appl. Phys. 32 (3) (1961) 510–519, https://doi.org/10.1063/1.1736034.
[9] O.D. Miller, E. Yablonovitch, S.R. Kurtz, Strong internal and external luminescence as solar cells approach the Shockley-Queisser limit, IEEE J. Photovoltaics 2 (3) (2012) 303–311, https://doi.org/10.1109/JPHOTOV.2012.2198434.
[10] J.F. Geisz, et al., Six-junction III–V solar cells with 47.1% conversion efficiency under 143 Suns concentration, Nat. Energy 5 (4) (Apr. 2020) 326–335, https://doi.org/10.1038/s41560-020-0598-5.
[11] M.A. Steiner, et al., Effects of Internal Luminescence and Internal Optics on V_{oc} and $J_{sc}$of III-V Solar Cells, IEEE J. Photovoltaics 3 (4) (Oct. 2013) 1437–1442, https://doi.org/10.1109/JPHOTOV.2013.2278666.
[12] D.J. Friedman, J.F. Geisz, M.A. Steiner, Analysis of multijunction solar cell current-voltage characteristics in the presence of luminescent coupling, IEEE J. Photovoltaics 3 (4) (2013) 1429–1436, https://doi.org/10.1109/JPHOTOV.2013.2275189.
[13] E. Lopez, et al., Experimental coupling process efficiency and benefits of back surface reflectors in photovoltaic multi-junction photonic power converters, Prog. Photovoltaics Res. Appl. 29 (4) (2021) 461–470, https://doi.org/10.1002/pip.3391.
[14] D.J. Friedman, J.F. Geisz, M.A. Steiner, Effect of luminescent coupling on the optimal design of multijunction solar cells, IEEE J. Photovoltaics 4 (3) (2014) 986–990, https://doi.org/10.1109/JPHOTOV.2014.2308722.
[15] G. Lush, M. Lundstrom, Thin film approaches for high-efficiency III-V cells, Sol. Cell. 30 (1–4) (1991) 337–344.

[16] A.W. Walker, et al., Impact of photon recycling and luminescence coupling on III–V single and dual junction photovoltaic devices, J. Photon. Energy 5 (1) (Sep. 2015) 053087, https://doi.org/10.1117/1.jpe.5.053087.
[17] M. Wilkins, C.E. Valdivia, A.M. Gabr, D. Masson, S. Fafard, K. Hinzer, Luminescent coupling in planar opto-electronic devices, J. Appl. Phys. 118 (2015) 143102, https://doi.org/10.1063/1.4932660.
[18] M.P. Lumb, M.A. Steiner, J.F. Geisz, R.J. Walters, Incorporating photon recycling into the analytical drift-diffusion model of high efficiency solar cells, J. Appl. Phys. 116 (19) (Nov. 2014) 19504, https://doi.org/10.1063/1.4902320.
[19] T. Sogabe, et al., Experimental characterization and self-consistent modeling of luminescence coupling effect in III-V multijunction solar cells, Appl. Phys. Lett. 103 (26) (Dec. 2013), https://doi.org/10.1063/1.4858970.
[20] M. Schauerte, O. Höhn, H. Helmers, Subcell spectral response determination for multi-junction photonic power converters based on negative bias I-V, in: *The 4th Optical Wireless and Fiber Power Transmission Conference*, PHOTONICS International Congress 2022, 2022.
[21] S.K. Reichmuth, G. Siefer, M. Schachtner, M. Mühleis, J. Hohl-Ebinger, S.W. Glunz, Measurement uncertainties in I-V calibration of multi-junction solar cells for different solar simulators and reference devices, IEEE J. Photovoltaics 10 (4) (Jul. 2020) 1076–1083, https://doi.org/10.1109/JPHOTOV.2020.2989144.
[22] M.A. Steiner, J.F. Geisz, Non-linear luminescent coupling in series-connected multijunction solar cells, Appl. Phys. Lett. 100 (25) (Jun. 2012), https://doi.org/10.1063/1.4729827.
[23] M.N. Beattie, et al., Subcell-resolved EQE method using reverse voltage biasing for multijunction photovoltaics with overlapping subcell absorptance, Prog. Photovoltaics Res. Appl. 33 (7) (Jul. 2025) 747–756, https://doi.org/10.1002/pip.3914.
[24] M. Schachtner, M.N. Beattie, S.K. Reichmuth, A. Wekkeli, G. Siefer, H. Helmers, Measuring the device-level EQE of multi-junction photonic power converters, Prog. Photovoltaics Res. Appl. 32 (11) (2024) 827–836, https://doi.org/10.1002/pip.3833.
[25] J.L. Balenzategui, A. Martí, Detailed modelling of photon recycling: application to GaAs solar cells, Sol. Energy Mater. Sol. Cell. 90 (7–8) (May 2006) 1068–1088, https://doi.org/10.1016/j.solmat.2005.06.004.
[26] Multijunction luminescent coupling (MJ-LC): Advanced luminescence. https://github.com/pwilso/mj-l. (Accessed 26 May 2026), https://doi.org/10.5281/zenodo.15185410.
[27] M.A. Steiner, J.F. Geisz, I. García, D.J. Friedman, A. Duda, S.R. Kurtz, Optical enhancement of the open-circuit voltage in high quality GaAs solar cells, J. Appl. Phys. 113 (12) (Mar. 2013), https://doi.org/10.1063/1.4798267.
[28] R.K. Ahrenkiel, Minority carrier lifetime in III-V semiconductors, in: R. K. Ahrenkiel, M.S. Lundstrom (Eds.), Semiconductors and Semimetals, . 39, Elsevier, 1993, p. 409, ch. 2.
[29] W. Van Roosbroek, W. Shockley, Photon-radiative recombination of electrons and holes in germanium, Phys. Rev. 94 (6) (1954) 1558–1560.
[30] V. Liu, S. Fan, S 4: a free electromagnetic solver for layered periodic structures, Comput. Phys. Commun. 183 (10) (2012) 2233–2244, https://doi.org/10.1016/j.cpc.2012.04.026.
[31] G.P. Forcade, et al., Multi-junction laser power converters exceeding 50% efficiency in the short wavelength infrared, Cell Rep. Phys. Sci. 6 (6) (2025) 102610, https://doi.org/10.1016/j.xcrp.2025.102610.
[32] M. Levinshtein, S. Rumyantsev, M. Shur, Handbook Series on Semiconductor Parameters, vol. 2, World Scientific Publishing Co., 1999.
[33] R.K. Ahrenkiel, B.M. Keyes, G.B. Lush, M.R. Melloch, M.S. Lundstrom, H. F. MacMillan, " Minority-carrier lifetime and photon recycling in n -GaAs ,", J. Vac. Sci. Technol. A: Vacuum, Surfaces, and Films 10 (4) (Jul. 1992) 990–995, https://doi.org/10.1116/1.577892.
[34] M.N. Beattie, H. Helmers, G.P. Forcade, C.E. Valdivia, O. Hohn, K. Hinzer, InP- and GaAs-Based photonic power converters under O-Band laser illumination: performance analysis and comparison, IEEE J. Photovoltaics (2022), https://doi.org/10.1109/JPHOTOV.2022.3218938.
[35] R.N. Hall, Electron-hole recombination in Germanium, Phys. Rev. 87 (1952) 387.
[36] M. Meusel, C. Baur, G. Létay, A.W. Bett, W. Warta, E. Fernandez, Spectral response measurements of monolithic GaInP/Ga(In)As/Ge triple-junction solar cells: measurement artifacts and their explanation, Prog. Photovoltaics Res. Appl. 11 (8) (Dec. 2003) 499–514, https://doi.org/10.1002/pip.514.
[37] M.A. Steiner, et al., Measuring IV curves and subcell photocurrents in the presence of luminescent coupling, IEEE J. Photovoltaics 3 (2) (2012) 879–887.
[38] H. Yoon, R.R. King, G.S. Kinsey, S. Kurtz, D.D. Krut, Radiative coupling effects in GaInP/GaAs/Ge multijunction solar cells, in: 3rd World Conference on Photovoltaic Energy Conversion, 2003, pp. 11–18.